



HAL
open science

Nonlinear Earthquake Response of Marine Sediments With Distributed Acoustic Sensing

Loïc Viens, Luis Fabian Bonilla, Zack J Spica, Kiwamu Nishida, Tomoaki Yamada, Masanao Shinohara

► **To cite this version:**

Loïc Viens, Luis Fabian Bonilla, Zack J Spica, Kiwamu Nishida, Tomoaki Yamada, et al.. Nonlinear Earthquake Response of Marine Sediments With Distributed Acoustic Sensing. *Geophysical Research Letters*, 2022, 49 (21), 18 p. 10.1029/2022gl100122 . hal-04402121

HAL Id: hal-04402121

<https://univ-eiffel.hal.science/hal-04402121v1>

Submitted on 18 Jan 2024

HAL is a multi-disciplinary open access archive for the deposit and dissemination of scientific research documents, whether they are published or not. The documents may come from teaching and research institutions in France or abroad, or from public or private research centers.

L'archive ouverte pluridisciplinaire **HAL**, est destinée au dépôt et à la diffusion de documents scientifiques de niveau recherche, publiés ou non, émanant des établissements d'enseignement et de recherche français ou étrangers, des laboratoires publics ou privés.

Public Domain

Nonlinear earthquake response of marine sediments with distributed acoustic sensing

Loïc Viens¹, Luis Fabian Bonilla², Zack J. Spica¹, Kiwamu Nishida³, Tomoaki Yamada³, and Masanao Shinohara³

¹Department of Earth and Environmental Sciences, University of Michigan, Ann Arbor, Michigan, USA

²Department of Geotechnical Engineering, Environment, Natural hazards and Earth sciences, Université

Gustave Eiffel, Marne-la-Vallée, France

³Earthquake Research Institute, The University of Tokyo, Tokyo, Japan

Key Points:

- AutoCorrelation Functions (ACFs) of earthquakes recorded by a DAS experiment exhibit phase delays with increasing ground motions
- ACF phase delays are converted to relative velocity drops in the medium that characterize soil nonlinearity
- DAS is used to infer the nonlinear behavior of soils with an unprecedented spatial resolution

Corresponding author: Loïc Viens, lviens@umich.edu

This article has been accepted for publication and undergone full peer review but has not been through the copyediting, typesetting, pagination and proofreading process, which may lead to differences between this version and the [Version of Record](#). Please cite this article as [doi: 10.1029/2022GL100122](https://doi.org/10.1029/2022GL100122).

This article is protected by copyright. All rights reserved.

Abstract

Soft sediment layers can significantly amplify seismic waves from earthquakes. Large dynamic strains can trigger a nonlinear response of shallow soils with low strength, which is characterized by a shift of resonance frequencies, ground motion deamplification, and in some cases, soil liquefaction. We investigate the response of marine sediments during earthquake ground motions recorded along a fiber-optic cable offshore the Tohoku region, Japan, with Distributed Acoustic Sensing (DAS). We compute AutoCorrelation Functions (ACFs) of the ground motions from 105 earthquakes in different frequency bands. We detect time delays in the ACF waveforms that are converted to relative velocity changes (dv/v). dv/v drops, which characterize soil nonlinearity, are observed during the strongest ground motions and exhibit a large variability along the cable. This study demonstrates that DAS can be used to infer the dynamic properties of the shallow Earth with an unprecedented spatial resolution.

Plain Language Summary

Seismic waves from earthquakes are amplified by shallow and soft sediment layers of the Earth. This amplification is linear for weak seismic waves, but can become highly nonlinear during strong ground motions. Nonlinear soil response, which can lead to a complete failure of the ground through soil liquefaction, threatens the safety of human-made constructions and needs to be accurately characterized. We study the response of marine sediments offshore the Tohoku region in Japan using earthquake data recorded along a fiber-optic cable with Distributed Acoustic Sensing (DAS). We use an autocorrelation approach to analyze the ground motions from 105 earthquakes recorded by thousands of DAS channels. We detect a clear nonlinear behavior of shallow sediments during the strongest ground motions. Moreover, we show that soil nonlinearity significantly varies along the cable. Our methodology could easily be applied to earthquake DAS data recorded in populated and seismically active regions to help understand better the dynamic behavior of shallow soils.

1 Introduction

Local geological conditions can significantly impact the propagation of incoming seismic waves from earthquakes. In particular, shallow, soft, and unconsolidated sediment layers are well known to amplify earthquake ground motions (Sanchez-Sesma, 1987), which can lead to catastrophic events such as during the 1985 moment magnitude (M_w) 8.0 Michoacán earthquake in Mexico (Anderson et al., 1986; Campillo et al., 1989). When subjected to weak dynamic strains (i.e., less than 10^{-4} and 10^{-8} for field observations and laboratory experiments, respectively; Ishihara, 1996; TenCate et al., 2004), shallow soils linearly amplify seismic waves. During large dynamic strains, however, soft sediments can behave nonlinearly (e.g., Field et al., 1997; Ostrovsky & Johnson, 2001). Soil nonlinearity is generally characterized by a relative reduction of the high-frequency ground-motion amplification, which is related to an increase of damping in the medium, and a shift of the resonance frequency to lower frequencies due to a reduction of the shear modulus (Beresnev & Wen, 1996; Brunet et al., 2008; Bonilla et al., 2011; Lyakhovsky et al., 2009; Zaitsev et al., 2005). In some cases, large dynamic strains can trigger a complete failure of cohesionless and saturated shallow sediments through soil liquefaction (Kramer, 1996), which can have disastrous consequences for human infrastructures as observed during the 1964 Niigata (Japan, Ohsaki, 1966) and 2010–2011 Christchurch (New Zealand, Quigley et al., 2013) earthquakes. Therefore, characterizing the nonlinear response of shallow sediments to earthquake ground motions is critical for mitigating seismic risk.

Several empirical methods have been developed to assess the response of soils to ground motions. A classical approach relies on computing the spectral ratio of earthquakes recorded at a soft-soil site and a nearby reference rock site (Borcherdt, 1970; Field & Ja-

66 cob, 1995; Bonilla et al., 1997). However, a reference site may not always be available
67 in the vicinity of the site of interest. Another approach consists in using pairs of surface-
68 borehole stations to detect potential soil nonlinear elastic behavior between the two sensors
69 (Bonilla et al., 2011; Minato et al., 2012; Nakata & Snieder, 2011; Régnier et al.,
70 2013; Sawazaki et al., 2006; Takagi et al., 2012; Wen et al., 1995). While this technique
71 isolates the shallow subsurface response from the earthquake source and path effects, pairs
72 of surface-borehole instruments are expensive to install and their low spatial coverage
73 does not capture small-scale lateral variations.

74 AutoCorrelation Functions (ACFs) calculated from data recorded by surface seis-
75 mometers yield the reflectivity response of the underlying elastic structure (Claerbout,
76 1968; Wapenaar, 2003). This technique has been primarily applied to image interfaces
77 with strong seismic impedance contrasts using earthquake (Delph et al., 2019; Pham &
78 Tkalčić, 2017; Tork Qashqai et al., 2019; Viens, Jiang, & Denolle, 2022) and ambient seis-
79 mic field (ASF; Gorbатов et al., 2013; Ito et al., 2012; Kennett, 2015; Saygin et al., 2017;
80 Spica, Nishida, et al., 2020; Viens, Jiang, & Denolle, 2022) datasets recorded onshore.
81 Repeated ACF computations through time from continuous ASF time series have also
82 been used to monitor temporal seismic velocity changes in the subsurface in different en-
83 vironments, such as volcanic (De Plaen et al., 2016; Sens-Schönfelder & Wegler, 2006;
84 Yates et al., 2019) and earthquake source (Hobiger et al., 2014; Ohmi et al., 2008; We-
85 gler et al., 2009) regions. However, the partitioning of body and surface waves in ACFs
86 computed from the ASF is generally unknown and hinders the interpretation of the mea-
87 sured velocity changes (Nakahara, 2015). To ease the interpretation, ACFs have also been
88 computed from earthquake P-, S-, or coda-wave windows (Bonilla et al., 2019; Bonilla
89 & Ben-Zion, 2020; Nakahara, 2015; Qin et al., 2020). Bonilla and Ben-Zion (2020) showed
90 that the first negative peak of ACFs calculated during earthquake ground motions cor-
91 responds to the seismic-wave two-way travel time between the sensor and the first ma-
92 jor interface below the station, and captures the soil nonlinear response. Moreover, Bonilla
93 et al. (2019) and Qin et al. (2020) showed that the response of the shallow subsurface
94 obtained from ACFs at surface stations yields a similar estimation of the soil nonlinear
95 behavior as that from a surface-borehole station configuration. In other words, ACFs
96 can isolate the site response term from the earthquake source and path effects, making
97 single-component stations a powerful tool for analyzing shallow sediment nonlinear be-
98 havior.

99 Mapping local site effects with data-driven techniques remains challenging due to
100 the large density of seismometers needed to capture complex spatial variations of the seis-
101 mic wavefield. In some cases, a large station coverage can be nearly impossible to attain
102 due to environmental or physical constraints, especially in urban and underwater areas.
103 Nevertheless, recent technological advances in Distributed Acoustic Sensing (DAS) of-
104 fer an unprecedented opportunity to measure the Earth's vibrations over tens of kilo-
105 meters with a dense spatial resolution ($\sim 1\text{--}50$ m) by turning ground-coupled fiber-optic
106 cables into arrays of sensors (Hartog, 2017). DAS uses an optoelectrical interrogator to
107 probe fibers with a laser sending thousands of short pulses of light every second. As each
108 pulse of light travels down the fiber, some of the light is reflected back to the interroga-
109 tor in a process known as Rayleigh backscattering. External forcing, such as seismic waves,
110 generate phase shifts of the back-scattered Rayleigh light, which are measured by the
111 interrogator. The measured phase shifts are finally linearly converted to longitudinal strain
112 (or strain rate) along the cable over a sliding spatial distance (i.e., the gauge length). Both
113 fit-to-purpose and existing fiber-optic telecommunication cables have been used to record
114 high-fidelity earthquake wavefields (Lellouch et al., 2019; Lior et al., 2021; Spica, Per-
115 ton, et al., 2020; Spica et al., 2022; Wang et al., 2018; Zeng et al., 2017). One great ad-
116 vantage of telecommunication fibers is that they have been widely deployed, from the
117 oceans' bottom to nearly every street in large developed cities, to sustain our modern
118 telecommunication network. Therefore, DAS could complement expensive urban and off-

119 shore seismic array deployments by probing existing telecommunication cables to cap-
120 ture the full extent of earthquake wavefields.

121 Nonlinear behavior of marine sediments during earthquake ground motions has been
122 observed with sparse ocean bottom seismometers (Dhakal et al., 2017; Kubo et al., 2019).
123 This study focuses on capturing the fine spatial resolution of the response of shallow ma-
124 rine sediments to 105 earthquakes recorded along a telecommunication cable offshore the
125 Sanriku coast in Japan by a DAS experiment (Figures 1a–b). After filtering the data into
126 different frequency bands, we calculate ACFs from the earthquake ground motions to
127 infer the soil response at different depths. We detect changes in the ACF time series that
128 are converted to relative velocity changes to characterize the soil linear and nonlinear
129 regimes below each DAS channel. We show that the relative velocity changes exhibit spa-
130 tial variations along the cable and are frequency dependent. We finally discuss our re-
131 sults and the potential of DAS for extracting soil parameters with unprecedented spa-
132 tial resolution.

133 2 Data and Methods

134 2.1 DAS data

135 The Earthquake Research Institute, The University of Tokyo, operates an ocean-
136 bottom observatory composed of three 3-component accelerometers and two tsunami me-
137 ters offshore the Sanriku Coast (Figure 1b; Kanazawa & Hasegawa, 1997; Shinohara et
138 al., 2021, 2022). The data recorded by the instruments are streamed in real-time to the
139 landing station located in the city of Kamaishi through a submarine telecommunication
140 cable. The cable contains six dark (unused) dispersion-shifted single-mode optical fibers
141 with a wavelength of 1,550 nm, which are suitable for DAS measurements. The first 47.7
142 km of the cable are relatively straight and buried under 0.6–0.7 m of sediments, which
143 should guarantee a good coupling with the surrounding medium. Moreover, the relatively
144 weak levels of shaking analyzed in this study (i.e., peak strain $< 10^{-7}$ or peak ground
145 acceleration < 1 cm/s/s) should not generate fiber movements that could impact the
146 recorded seismic waves (Nakamura & Hayashimoto, 2018).

147 An AP Sensing N5200A DAS interrogator unit (Cedilnik et al., 2019) probed one
148 of the dark fibers between November 18 and December 2, 2019, and recorded continu-
149 ous data over the first 70 km of the cable with a sampling rate of 500 Hz. The gauge length
150 and spatial sampling are set to 40 m and 5.1 m, respectively. The DAS system recorded
151 hundreds of earthquakes during the two weeks of measurement. We first convert the raw
152 DAS data to strain (Shinohara et al., 2022) and focus on the ground motions from 105
153 earthquakes that are clearly recorded by all DAS channels (Figure 1a–b). The velocity
154 magnitude (M_V , determined from the amplitude data recorded by short-period veloc-
155 ity seismometers; Kanbayashi & Ichikawa, 1977) of the earthquakes ranges between 1.0
156 and 5.3, and we show the strain waveforms of a M_V 2.5 earthquake in Figure 1c. This
157 event occurred on November 28, 2019 at 14:17:32UTC at a depth of 30 km. Clear P- and
158 S-wave arrivals can be observed at most channels as well as locally generated surface waves
159 that significantly extend the ground motion duration.

160 2.2 Autocorrelation functions and relative velocity changes

161 For each earthquake and each DAS channel, we compute the time derivative of the
162 strain data to retrieve strain-rate waveforms, which are proportional to acceleration time
163 series. We bandpass filter the strain-rate data between 2 and 30 Hz (all filters are two-
164 pass four-pole Butterworth bandpass filters) and select a fixed 15-s window starting 5
165 s before the earthquake absolute maximum amplitude. We then bandpass filter the raw
166 strain-rate waveforms into 18 frequency bands (e.g., 3–6, 4–8, ..., 20–40 Hz), apply 1-bit
167 normalization to the data (Bensen et al., 2007), and compute ACFs over the fixed 15-

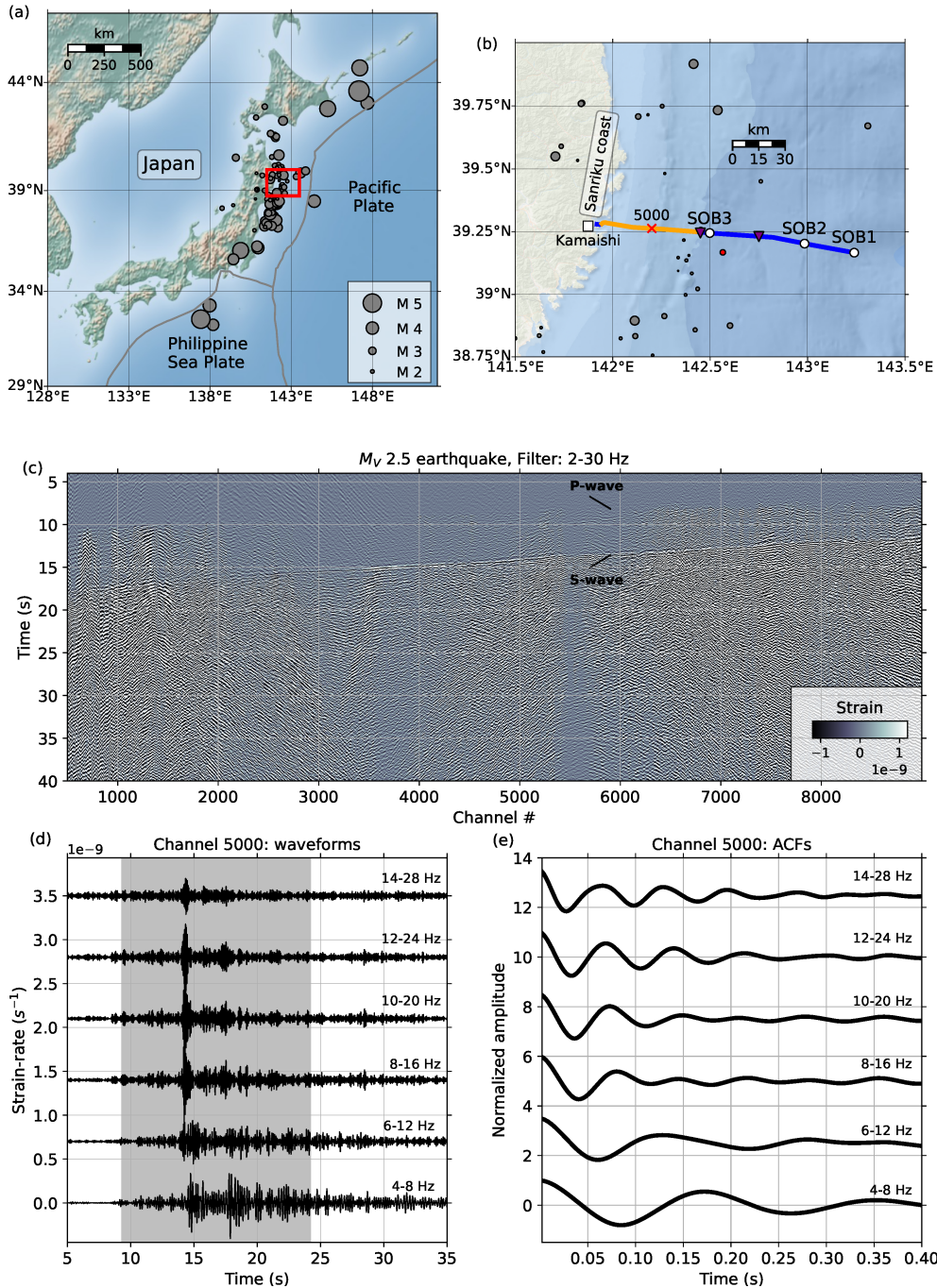


Figure 1. (a) Topographic map of Japan and its surroundings including 105 earthquakes. The red rectangle denotes the region shown in (b). (b) Bathymetric map offshore the Sanriku coast including the seafloor cable observation system. The orange line denotes the buried section of the cable between channels 500 and 9000 and the location of channel 5000 is indicated by the red cross. The white circles and purple inverted triangles show the positions of the accelerometers and tsunami-meters, respectively. The location of the M_V 2.5 event (red circle), for which the waveforms are shown in (c), and that of other nearby earthquakes (gray circles) are highlighted. The magnitude scale is the same as in (a). (c) Strain waveforms of the M_V 2.5 event bandpass filtered between 2 and 30 Hz between channels 500 and 9000. Waveform amplitudes are clipped for visibility. (d) Strain-rate waveforms of the M_V 2.5 earthquake bandpass filtered in different frequency bands at channel 5000. The gray area denotes the time period over which the ACFs are calculated. (e) Amplitude normalized ACFs computed from the waveforms shown in (d).

s window using a phase correlation method in the frequency domain (Schimmel & Paulssen, 1997; Ventosa et al., 2019). We show the bandpass filtered strain-rate waveforms of the M_V 2.5 earthquake together with their corresponding ACFs at channel 5000 in Figures 1d and 1e, respectively.

As the ACFs are calculated around the S-wave direct arrival, we expect their first negative peak to capture the S-wave two-way travel time between the cable and an interface with a strong seismic impedance contrast (Bonilla & Ben-Zion, 2020). Nevertheless, a theoretical/numerical study should explore the potential effects of ACF near-zero-time-lag source effects on the S-wave two-way travel time, especially in offshore environments. In addition, the different frequency bands allow us to sample different depth of the media, with low-frequency bandpass filtered ACFs displaying later arrivals as they sample deeper media compared to high-frequency ACFs. However, detailed knowledge of the subsurface is required to precisely determine the depth sampled by ACFs.

The 105 earthquake waveforms analyzed in this study generated various levels of dynamic strain along the cable. In Figures 2a-d, we show the ACFs calculated for all the earthquakes after bandpass filtering the strain-rate data between 10–20 Hz and 15–30 Hz at channels 5000 and 7000. We also show the dynamic peak strains computed as the absolute maximum amplitude of the bandpass filtered strain data in Figures 2e-f. For both frequency bands, the ACF first negative peaks exhibit similar lag times for weak dynamic strains ($< \sim 5 \times 10^{-10}$), but clear delays can be observed for larger dynamic peak strains.

Soil nonlinear behavior during ground motions delays the ACF first negative peak and can therefore be interpreted as a velocity reduction in the medium (Bonilla & Ben-Zion, 2020). Under the assumption that the changes in the medium are uniformly distributed, we can estimate the relative velocity changes (dv/v) of each ACF with respect to a reference ACF with the stretching method (Lobkis & Weaver, 2003; Sens-Schönfelder & Wegler, 2006) as

$$\tau = \frac{dt}{t} = -\frac{dv}{v}, \quad (1)$$

where τ , dt/t , and dv/v are the stretching coefficient, the relative time shift, and the relative velocity change, respectively. The dv/v changes are computed in several steps to estimate measurement errors. For each channel and each frequency band, we first compute 100 reference ACFs by randomly stacking between 5 and 20 ACFs computed during the 20 weakest dynamic peak strains. We then select a time window that corresponds to 75% of the inverse of each lower cutoff frequency (e.g., the first 0.25 s of the ACF for the 3-6 Hz frequency band) to focus on the first negative peak of the ACFs. We stretch/compress the selected window of each reference ACF to find the stretching coefficient that maximizes the fit with each earthquake ACF, and therefore measure dv/v changes. The stretching is performed in two steps; we first use ten values uniformly distributed between -50 and 50% of stretching to find an initial guess of the stretching coefficient, and then refine the measurement by interpolating the stretched waveforms 500 times between the neighboring values (similar to Viens et al., 2018). For each channel and each frequency band, we finally compute the mean and one standard deviation from the mean of the 100 dv/v measurements to estimate errors.

3 Results

We show the mean of the dv/v measurements for all the frequency bands and earthquakes for two ranges of channels in Figures 3a-b, and the corresponding uncertainties in Figure S1. While the soil nonlinear response can rapidly evolve spatially, we display the combined results at 10 neighboring channels (i.e., over 51 m) between channels 5000–5010 and 7000–7010 for visibility. For dynamic peak strains smaller than $\sim 5 \times 10^{-10}$, dv/v measurements are generally equal to zero for all frequency bands at both locations, which

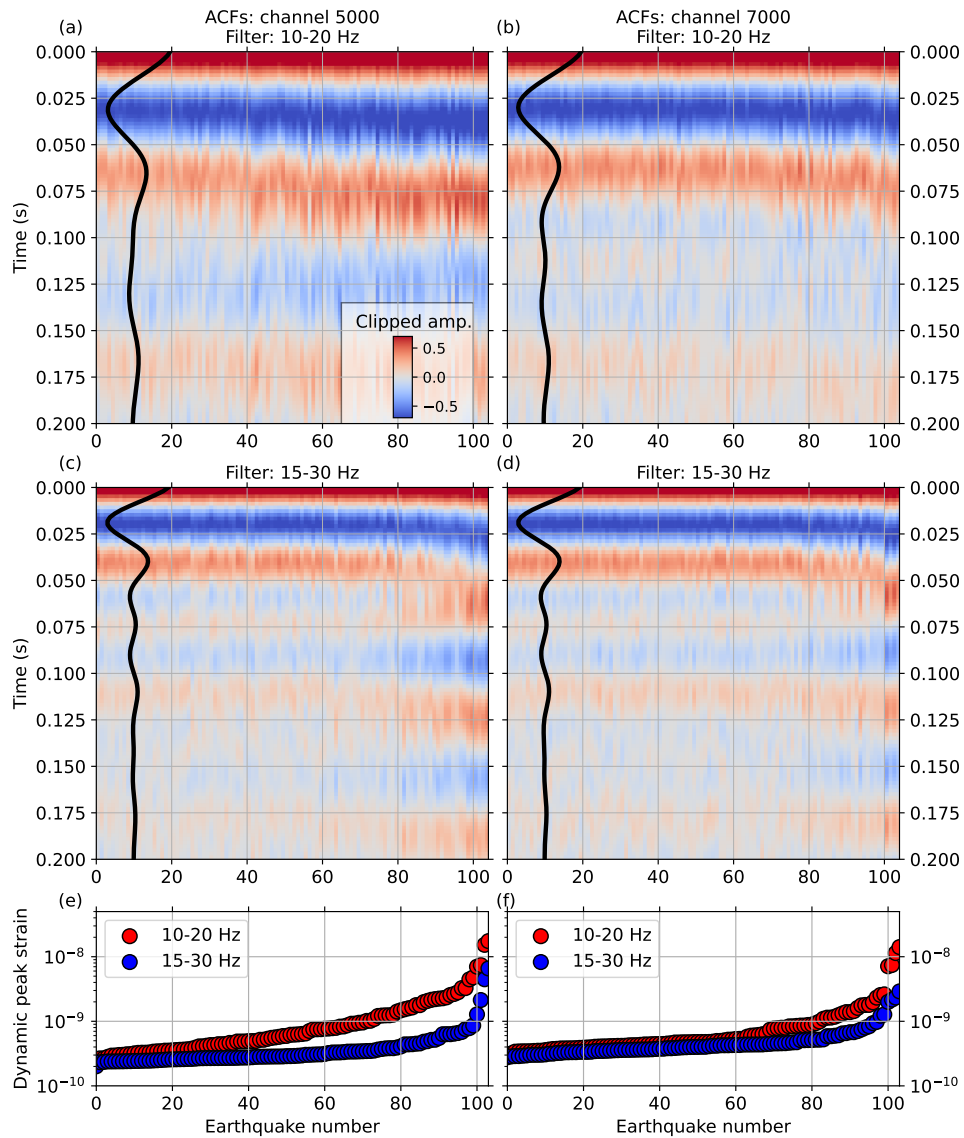


Figure 2. ACFs computed from the 105 earthquakes bandpass filtered between 10 and 20 Hz at channels (a) 5000 and (b) 7000. The amplitude of the data is clipped for visibility. (c–d) Same as (a–b) in the 15–30 Hz frequency band. (e–f) Dynamic peak strains after bandpass filtering the earthquake strain waveforms between 10–20 Hz and 15–30 Hz at channels 5000 and 7000, respectively. The ACFs in (a–d) are sorted by the increasing dynamic peak strain values shown in (e–f).

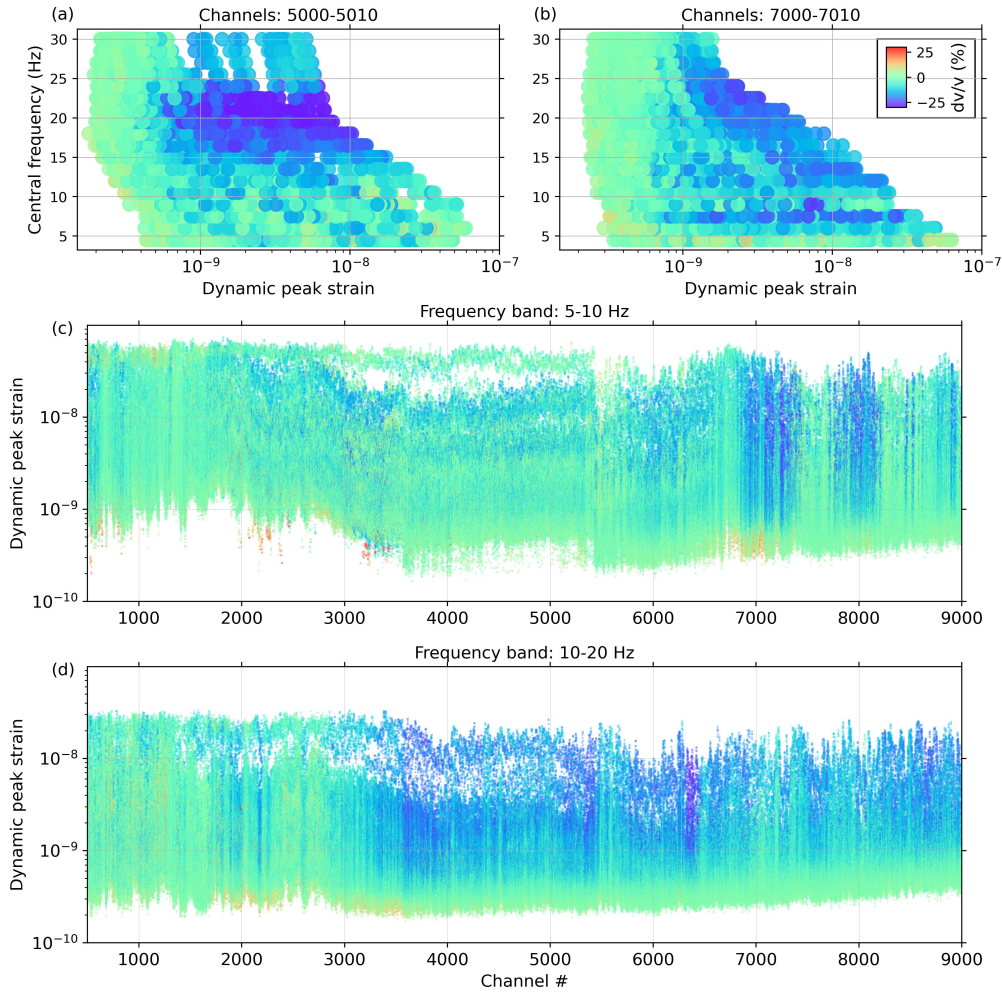


Figure 3. (a) Mean dv/v measurements at channels 5000–5010 for the 18 frequency bands and the 105 earthquakes. Dynamic peak strains are computed for each event and each channel after bandpass filtering the strain data. The central frequency is the bandpass filter central frequency. (b) Same as (a) at channels 7000–7010. (c) Mean dv/v measurements from the ACFs computed from the 105 earthquakes bandpass filtered between 5 to 10 Hz between channels 500 and 9000 as a function of the dynamic peak strain. (d) Same as (c) for the 10–20 Hz frequency band. The dv/v color-scale shown in (b) is the same for all panels.

218 indicates that there is no change in the medium. However, clear dv/v drops can be ob-
 219 served in different frequency bands with increasing dynamic peak strains at the two lo-
 220 cations. For example, we primarily observe dv/v reductions between central frequencies
 221 (i.e., the central frequency of the bandpass filter: 15 Hz for the 10–20 Hz bandpass fil-
 222 ter) of 15–24 Hz for channels 5000–5010 and 12–28 Hz for channels 7000–7010. More-
 223 over, we also note that the intensity of the dv/v changes varies, with larger changes at
 224 channels 5000–5010 compared to those at channels 7000–7010.

225 Spatial variations of the relative velocity changes can also be detected along the
 226 cable with the high density of DAS channels. In Figures 3c-d, we show the mean dv/v
 227 measurements along the cable in two frequency bands (5–10 and 10–20 Hz), which ex-
 228 hibit clear spatial differences. In the 5–10 Hz frequency band, almost no dv/v changes
 229 can be observed between channels 500 and 6900, even during the strongest dynamic peak
 230 strains. However, we detect clear dv/v drops for dynamic peak strains above 10^{-9} be-
 231 tween channels 6900 and 8200. In the 10–20 Hz frequency band, almost no changes are
 232 found between channels 500–3500, but large dv/v drops are observed after channel 3500
 233 for dynamic peak strains larger than $\sim 10^{-9}$.

234 To isolate and investigate the average sediment response during strong ground mo-
 235 tions, we also compute dv/v measurements between each reference ACF (i.e., the stack
 236 of the ACFs computed during the 20 weakest dynamic peak strains) and a stack of the
 237 ACFs computed during the 10 largest dynamic peak strains (More details about uncer-
 238 tainty computation in Text S2). Mean dv/v changes between weak and strong ground
 239 motion ACFs exhibit clear spatial and frequency variations (Figure 4a). Between chan-
 240 nels 500 and 2000, we do not detect any large dv/v changes. However, we observe spa-
 241 tial variations of the dv/v reductions at central frequencies above 15 Hz between chan-
 242 nels 2000 and 9000. We also observe clear dv/v changes at frequencies below 15 Hz be-
 243 tween channels 6300 and 9000. Note that the largest dv/v values are not correlated with
 244 the highest dynamic peak strain values (Figure 4b). Therefore, the coherent spatial changes
 245 across frequency bands highlight the sensitivity of DAS ACFs to local site conditions.

246 The amplitude of dv/v reductions is expected to increase with increasing dynamic
 247 peak strains. In Figures 4c-e, we show the dv/v measurements calculated between the
 248 weak and strong ground motion ACFs as a function of the dynamic peak strains in three
 249 frequency bands (3–6, 15–30, and 20–40 Hz). We only show the results at 650 locations
 250 between channels 1700–8200 as we average the dv/v and dynamic peak strain values over
 251 10 neighboring channels (e.g., channels 1995–2005 for channel 2000). This step is per-
 252 formed to compare our results with local site condition data from a velocity model of
 253 the region, as discussed below. For the three frequency bands, the largest dynamic peak
 254 strains are typically observed before channel 3000 and we generally see an increase of
 255 the dv/v drops with increasing dynamic peak strains. In the 15–30 Hz frequency band,
 256 the dv/v values at the beginning of the cable (before channel 4000) do not behave in the
 257 same way as channels located further away from the coast, as shown by the relatively
 258 scattered dv/v values in Figure 4d.

259 In Figures 4f–h, we show the dv/v measurements at the same 650 locations as a
 260 function of the average S-wave velocity in the first 30 m of the ground (V_{S30}) obtained
 261 from the velocity model derived by Viens, Perton, et al. (2022). The Viens, Perton, et
 262 al. (2022) model was obtained by inverting Rayleigh wave phase velocity dispersion curves
 263 calculated by seismic interferometry using virtual sources located every 10 channels (e.g.,
 264 51 m). We compute V_{S30} from the 650 locations of the velocity model and apply a smooth-
 265 ing of the V_{S30} values over 5 locations. We observe a decrease of dv/v changes with de-
 266 creasing V_{S30} values in the 20–40 Hz frequency band. However, we do not observe any
 267 clear correlation between V_{S30} and the dv/v results in the 3–6 and 15–30 Hz frequency
 268 bands.

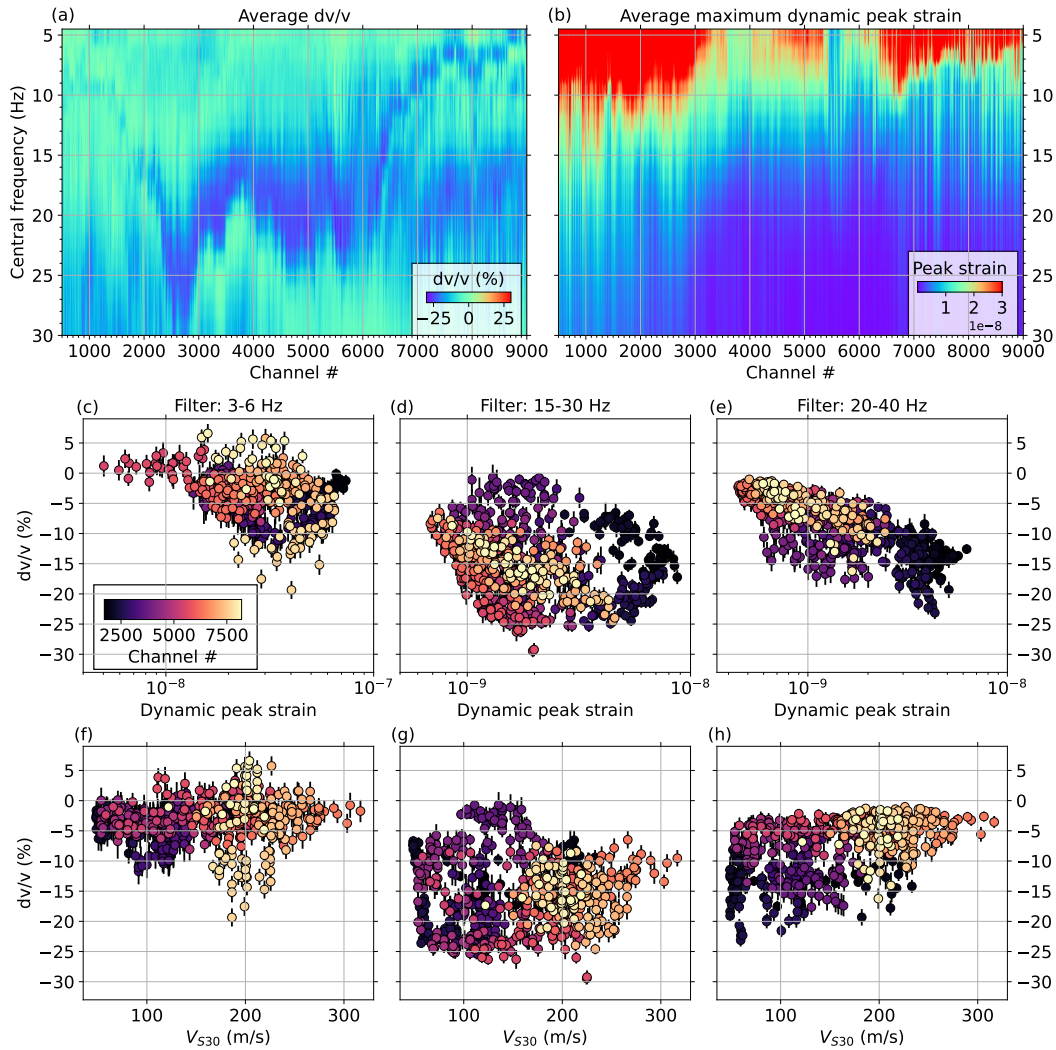


Figure 4. (a) Mean dv/v values computed between weak and strong ground motion ACFs at each channel and each frequency band. (b) Average maximum dynamic peak strain over the 10 largest peak strains at each channel and each frequency band. (c) Relative velocity changes as a function of the filtered dynamic peak strain in the 3-6 Hz frequency band. The error bars represent the one standard deviation from the mean of the dv/v measurements (Figure S2). (d–e) Same as (c) for the 15-30 and 20-40 Hz frequency bands. (f) Relative velocity changes as a function of the average S-wave velocity within the first 30 m of the ground (V_{S30}) for the 3-6 Hz frequency band. (g–h) Same as (f) for the 15-30 and 20-40 Hz frequency bands. In (c–h), the color-scale corresponds to the channel number.

4 Discussion

While larger dynamic peak strains generally correlate with larger dv/v drops, the correlation with V_{S30} is weaker or even nonexistent. This contrasts with the study by Yang et al. (2022), who observed a good correlation between stronger site effects and slower shallow S-wave velocities. Three hypotheses can explain this behavior. First, the velocity model, which was obtained from ASF cross-correlation functions spanning over 2 km (i.e., 400 channels), only captures a smoothed representation of the shallow Earth structure. Therefore, V_{S30} from the velocity model may not fully capture the structural changes that can rapidly occur at shallow depths. Secondly, we expect the ACFs to have different depth sensitivities based on their frequency ranges. Therefore, a single parameter, namely V_{S30} , does not account for such depth sensitivity variations. Thirdly, while an accurate value of V_{S30} can be useful for some geotechnical engineering purposes, it may not be the best parameter to explain the intensity of dv/v drops. For example, in a 30 m profile composed of a very shallow and soft sediment layer overlaying a stiffer material, nonlinearity is expected to only occur in the first layer. Therefore, a complete velocity profile of each site is likely to be more informative than a summarizing parameter (i.e., V_{S30} ; Bonilla et al., 2021), and future work should focus on refining the shallow velocity structure.

Earthquake source duration increases as seismic moment rises, which expands the lower frequency content of the recorded seismic waves in the far field (Brune, 1970). Such frequency content changes can potentially create a time shift of the ACFs first negative arrivals and therefore introduce source-related artifacts in the dv/v measurements. However, earthquake source effects are likely small compared to nonlinear effects in this study for three reasons. First, Qin et al. (2020) showed that ACFs calculated from earthquake waveforms recorded at a surface station at a sedimentary site display similar dv/v values as those computed between borehole and surface stations, which remove the contribution of the earthquake source and path effects. This demonstrates that nonlinear effects at sedimentary sites are generally significantly stronger than earthquake source effects. Secondly, larger magnitude earthquakes do not necessarily cause larger ACF time delays (Figure S3). Thirdly, earthquake source effects are minimized by the range of earthquake magnitudes used to compute the reference ACFs. Each reference ACF is obtained by stacking 20 ACFs from earthquake velocity magnitudes primarily ranging between 1.4 and 4.3 (Figure S4), which overlaps the 1.4-5.3 magnitude range of all the earthquakes analyzed in this study. While this processing step likely smooths earthquake source effects, all dv/v measurements are made with respect to a reference waveform, and are therefore not absolute. Yet, earthquake source effects could become significant if reference ACFs are exclusively computed from small magnitude earthquakes.

While the dynamic strains analyzed in this study are relatively weak, we observe significant relative velocity changes from the ACFs, which indicate a nonlinear response of marine sediments. Due to the weak levels of shaking, soil nonlinearity only occurs during the passing of seismic waves, and no long-term effects can be detected. Nevertheless, the nonlinearity thresholds of strain levels obtained along the cable are consistent with those from laboratory experiments (Pasqualini et al., 2007; Remillieux et al., 2017; Ten-Cate et al., 2004), although larger dv/v drops are observed in this study. This difference could be explained by the different materials being analyzed (e.g., sandstone versus marine sediments), with marine sediments having a higher susceptibility to nonlinearity. Our dv/v results are also comparable to those from (Bonilla & Ben-Zion, 2020) who observed dv/v drops of a few percent during small local earthquakes in California. To further validate our approach, we also compute ACFs from earthquake data recorded by the horizontal accelerometer along the axis of the cable from the SOB3 station (Figure S5). The ACFs from the SOB3 station exhibit similar features, with a nonlinearity threshold of the same order as that obtained with the DAS data, which validates our approach.

321 The dynamic peak strains recorded by the DAS channels are in the direction of the
322 cable; however, DAS has different theoretical sensitivities depending on the type of seis-
323 mic waves and their incidence angles (Martin et al., 2021). For example, DAS records
324 from earthquakes occurring at a 90-degree angle from the direction of the cable are ex-
325 pected to exhibit less energy than events happening along the axis of the cable. More-
326 over, the relatively long gauge length (i.e., 40 m) used to record the DAS data could cre-
327 ate notches in the frequency spectrum between 2 and 40 Hz (Dean et al., 2017). Nev-
328 ertheless, the steep subduction zone in the Tohoku region (Hayes et al., 2018) combined
329 with shallow and slow sediment layers interfere with the propagation of seismic waves,
330 which likely arrive with almost vertical angles to the cable. This translates into high ap-
331 parent velocities of all earthquake wavefields recorded by the cable (e.g., Figure 1c), which
332 limits both the azimuthal and gauge length effects on the recorded data. We further con-
333 firm this point by comparing the maximum amplitudes of DAS and SOB3 data during
334 the 105 earthquakes considered in this study in Figure S6. Both datasets exhibit sim-
335 ilar maximum amplitudes with respect to azimuth angles to the earthquake epicenters,
336 which confirms that there is no noticeable azimuthal effect for the DAS data.

337 The largest ground motions during the two-week experiment occurred during a M_V
338 5.6, which occurred 50 km east of the SOB3 station (Figure S7). However, the ampli-
339 tude of the DAS data clipped and are therefore not usable in our analysis. The data clip-
340 ping issue is caused by rapid phase changes that occurred during strong ground motions,
341 which wrap the signal's phase. To reduce clipping effects and improve the dynamic range
342 of DAS experiments, one can increase the laser pulse rate frequency, which would limit
343 the maximum distance that the DAS interrogator can sample, and/or reduce the gauge
344 length, which could result in a decrease of the SNR of the recorded wavefield (Mellors
345 et al., 2022). Despite these drawbacks, a better tuning of the DAS parameters could al-
346 low us to record strong ground motions that are likely to trigger stronger nonlinear soil
347 responses.

348 5 Conclusions

349 We analyzed the ground motions of 105 earthquakes recorded along a fiber-optic
350 cable during a two-week DAS campaign offshore Japan. We computed ACFs of earth-
351 quake ground motions and detected relative velocity changes in the marine sediments
352 surrounding the cable from the ACFs. Large drops of dv/v are observed along the ca-
353 ble and are typical of nonlinear behavior of the medium. Moreover, the dv/v changes
354 are frequency and spatially dependent, highlighting the sensitivity of DAS ACFs to the
355 shallow Earth structure.

356 This study demonstrates that earthquakes recorded by DAS can be used to char-
357 acterize soil nonlinearity during ground motions. This could be critical for fiber-optic
358 cables being considered for earthquake early warning purposes, as soil nonlinearity im-
359 pacts the amplitude and frequency content of the recorded wavefield and could bias rapid
360 magnitude estimations. Finally, the ACF approach could easily be applied to other DAS
361 datasets recorded in populated regions located on top of sedimentary basins, such as Mex-
362 ico City and Los Angeles, to better characterize seismic hazard.

363 Acknowledgments

364 We thank Takeshi Akuhara for providing useful information about DAS measurements.
365 We thank *Fujitsu* for cooperating with the Earthquake Research Institute (ERI), The
366 University of Tokyo, for the DAS measurement campaigns. We are grateful to the Ed-
367 itor Daoyuan Sun and two anonymous reviewers for providing helpful comments that im-
368 proved this study. **Funding:** This project was partly supported by the discretionary bud-
369 get of the director of ERI. The observations were carried out as part of the Earthquake
370 and Volcano Hazards Observation and Research Program by the Ministry of Education,

371 Culture, Sports, Science, and Technology of Japan. L.V. was supported by NSF award
 372 EAR2022716. Z.J.S acknowledges support from the Air Force Research Laboratory grant
 373 FA9453-21-2-0018. **Competing interests:** The authors declare that they have no com-
 374 peting interests.

375 **Open Research:** The data and codes developed to perform the technical analysis and
 376 to reproduce most figures are available at <https://doi.org/10.5281/zenodo.7044595>.
 377 All the Figures are plotted with Matplotlib (Hunter, 2007) and some of the data pro-
 378 cessing steps have been performed using ObsPy (Beyreuther et al., 2010).

379 References

- 380 Anderson, J. G., Bodin, P., Brune, J. N., Prince, J., Singh, S. K., Quaas, R., &
 381 Onate, M. (1986). Strong ground motion from the Michoacan, Mexico, earth-
 382 quake. *Science*, *233*, 1043–1049. doi: 10.1126/science.233.4768.1043
- 383 Bensen, G. D., Ritzwoller, M. H., Barmin, M. P., Levshin, A. L., Lin, F., Moschetti,
 384 M. P., ... Yang, Y. (2007). Processing seismic ambient noise data to obtain
 385 reliable broad-band surface wave dispersion measurements. *Geophys. J. Int.*,
 386 *169*, 1239–1260. doi: 10.1111/j.1365-246X.2007.03374.x
- 387 Beresnev, I. A., & Wen, K.-L. (1996). Nonlinear soil response—a reality? *Bull. Seis-*
 388 *mol. Soc. Am.*, *86*, 1964–1978. Retrieved from [http://bssa.geoscienceworld](http://bssa.geoscienceworld.org/content/86/6/1964)
 389 [.org/content/86/6/1964](http://bssa.geoscienceworld.org/content/86/6/1964)
- 390 Beyreuther, M., Barsch, R., Krischer, L., Megies, T., Behr, Y., & Wassermann, J.
 391 (2010, 05). ObsPy: A Python Toolbox for Seismology. *Seism. Res. Lett.*,
 392 *81*(3), 530–533. Retrieved from <https://doi.org/10.1785/gssrl.81.3.530>
 393 doi: 10.1785/gssrl.81.3.530
- 394 Bonilla, L. F., & Ben-Zion, Y. (2020, 11). Detailed space–time variations of
 395 the seismic response of the shallow crust to small earthquakes from analy-
 396 sis of dense array data. *Geophys. J. Int.*, *225*(1), 298–310. Retrieved from
 397 <https://doi.org/10.1093/gji/ggaa544> doi: 10.1093/gji/ggaa544
- 398 Bonilla, L. F., Guéguen, P., & BenZion, Y. (2019, 01). Monitoring Coseismic
 399 Temporal Changes of Shallow Material during Strong Ground Motion with
 400 Interferometry and Autocorrelation. *Bulletin of the Seismological Society of*
 401 *America*, *109*(1), 187–198. doi: 10.1785/0120180092
- 402 Bonilla, L. F., Guéguen, P., & C., G. (2021, 30 August–1 September). Contribution
 403 of k-net and kik-net data to the monitoring of nonlinear properties of the shal-
 404 low crust. In *6th iaspei/iaee international symposium: Effects of surface geol-*
 405 *ogy on seismic motion*. Kyoto, Japan. Retrieved from <http://www.esg6.jp>
- 406 Bonilla, L. F., Steidl, J. H., Lindley, G. T., Tumarkin, A. G., & Archuleta, R. J.
 407 (1997). Site amplification in the san fernando valley, california: Variability of
 408 site-effect estimation using the s-wave, coda, and h/v methods. *Bull. Seismol.*
 409 *Soc. Am.*, *87*, 710. Retrieved from <http://dx.doi.org/>
- 410 Bonilla, L. F., Tsuda, K., Pulido, N., Régnier, J., & Laurendeau, A. (2011). Non-
 411 linear site response evidence of K-NET and KiK-net records from the 2011
 412 off the Pacific coast of Tohoku Earthquake. *Earth Planets Space*, *63*, 785–
 413 789. Retrieved from <http://dx.doi.org/10.5047/eps.2011.06.012> doi:
 414 10.5047/eps.2011.06.012
- 415 Borchardt, R. D. (1970). Effects of local geology on ground motion near san fran-
 416 cisco bay. *Bull. Seismol. Soc. Am.*, *60*, 29. Retrieved from [http://dx.doi](http://dx.doi.org/)
 417 [.org/](http://dx.doi.org/)
- 418 Brune, J. N. (1970). Tectonic stress and the spectra of seismic shear waves from
 419 earthquakes. *J. Geophys. Res.*, *75*, 4997–5009. doi: 10.1029/JB075i026p04997
- 420 Brunet, T., Jia, X., & Johnson, P. A. (2008). Transitional nonlinear elastic be-
 421 haviour in dense granular media. *Geophys. Res. Lett.*, *35*, L19308. Retrieved
 422 from <https://agupubs.onlinelibrary.wiley.com/doi/abs/10.1029/>

- 2008GL035264 doi: 10.1029/2008GL035264
- 423
424 Campillo, M., Gariel, J. C., Aki, K., & Sánchez-Sesma, F. J. (1989). Destructive
425 strong ground motion in Mexico city: Source, path, and site effects during
426 great 1985 Michoacán earthquake. *Bull. Seismol. Soc. Am.*, *79*, 1718–1735.
427 Retrieved from <http://www.bssaonline.org/content/79/6/1718.abstract>
- 428 Cedilnik, G., Lees, G., Schmidt, P., Herstrøm, S., & Geisler, T. (2019). Ultra-
429 long reach fiber distributed acoustic sensing for power cable monitoring.
430 *10th International Conference on Insulated Power Cables*. Retrieved from
431 [https://www.apsensing.com/fileadmin/Publication%20Files/Cedilnik](https://www.apsensing.com/fileadmin/Publication%20Files/Cedilnik_et.al._-2019-Jicable-Proceedings-E4-4-Ultralong-reach-DAS-.pdf)
432 [_et.al._-2019-Jicable-Proceedings-E4-4-Ultralong-reach-DAS-.pdf](https://www.apsensing.com/fileadmin/Publication%20Files/Cedilnik_et.al._-2019-Jicable-Proceedings-E4-4-Ultralong-reach-DAS-.pdf)
- 433 Claerbout, J. (1968). Synthesis of a layered medium from its acoustic transmission
434 response. *Geophysics*, *33*, 264–269. doi: 10.1190/1.1439927
- 435 Dean, T., Cuny, T., & Hartog, A. H. (2017). The effect of gauge length on
436 axially incident p-waves measured using fibre optic distributed vibra-
437 tion sensing. *Geophysical Prospecting*, *65*(1), 184–193. Retrieved from
438 <https://onlinelibrary.wiley.com/doi/abs/10.1111/1365-2478.12419>
439 doi: <https://doi.org/10.1111/1365-2478.12419>
- 440 Delph, J. R., Levander, A., & Niu, F. (2019). Constraining crustal properties us-
441 ing receiver functions and the autocorrelation of earthquake-generated body
442 waves. *Journal of Geophysical Research: Solid Earth*, *124*(8), 8981–8997. doi:
443 10.1029/2019JB017929
- 444 De Plaen, R. S. M., Lecocq, T., Caudron, C., Ferrazzini, V., & Francis, O. (2016).
445 Single-station monitoring of volcanoes using seismic ambient noise. *Geophys.*
446 *Res. Lett.*, *43*, 8511–8518. Retrieved from [http://dx.doi.org/10.1002/](http://dx.doi.org/10.1002/2016GL070078)
447 [2016GL070078](http://dx.doi.org/10.1002/2016GL070078) doi: 10.1002/2016GL070078
- 448 Dhakal, Y. P., Aoi, S., Kunugi, T., Suzuki, W., & Kimura, T. (2017). Assessment
449 of nonlinear site response at ocean bottom seismograph sites based on s-wave
450 horizontal-to-vertical spectral ratios: a study at the sagami bay area k-net
451 sites in japan. *Earth, Planets and Space*, *69*(1), 29. Retrieved from [https://](https://doi.org/10.1186/s40623-017-0615-5)
452 doi.org/10.1186/s40623-017-0615-5 doi: 10.1186/s40623-017-0615-5
- 453 Field, E. H., & Jacob, K. H. (1995, 08). A comparison and test of various
454 site-response estimation techniques, including three that are not reference-
455 site dependent. *Bull. Seismol. Soc. Am.*, *85*, 1127–1143. Retrieved from
456 <https://doi.org/10.1785/BSSA0850041127> doi: 10.1785/BSSA0850041127
- 457 Field, E. H., Johnson, P. A., Beresnev, I. A., & Zeng, Y. (1997, 12 11). Nonlinear
458 ground-motion amplification by sediments during the 1994 northridge earth-
459 quake. *Nature*, *390*, 599–602. Retrieved from [http://dx.doi.org/10.1038/](http://dx.doi.org/10.1038/37586)
460 [37586](http://dx.doi.org/10.1038/37586)
- 461 Gorbatov, A., Saygin, E., & Kennett, B. L. N. (2013, 12). Crustal properties from
462 seismic station autocorrelograms. *Geophys. J. Int.*, *192*(2), 861–870. doi: 10
463 .1093/gji/ggs064
- 464 Hartog, A. (2017). *An introduction to distributed optical fibre sensors*. CRC Press.
465 doi: <https://doi.org/10.1201/9781315119014>
- 466 Hayes, G. P., Moore, G. L., Portner, D. E., Hearne, M., Flamme, H., Furtney, M.,
467 & Smoczyk, G. M. (2018). Slab2, a comprehensive subduction zone geometry
468 model. *Science*, *362*(6410), 58–61. Retrieved from [https://www.science.org/](https://www.science.org/doi/abs/10.1126/science.aat4723)
469 [doi/abs/10.1126/science.aat4723](https://www.science.org/doi/abs/10.1126/science.aat4723) doi: 10.1126/science.aat4723
- 470 Hobiger, M., Wegler, U., Shiomi, K., & Nakahara, H. (2014). Single-station cross-
471 correlation analysis of ambient seismic noise: application to stations in the
472 surroundings of the 2008 iwate-miyagi nairiku earthquake. *Geophys. J. Int.*,
473 *198*, 90. Retrieved from <http://dx.doi.org/10.1093/gji/ggu115> doi:
474 10.1093/gji/ggu115
- 475 Hunter, J. D. (2007). Matplotlib: A 2d graphics environment. *Computing In Science*
476 *& Engineering*, *9*(3), 90–95. doi: 10.1109/MCSE.2007.55
- 477 Ishihara, K. (1996). *Soil behaviour in earthquake geotechnics*. Clarendon Press. Re-

- 478 trieved from <https://books.google.com/books?id=OXNxQgAACAAJ>
- 479 Ito, Y., Shiomi, K., Nakajima, J., & Hino, R. (2012). Autocorrelation analysis
- 480 of ambient noise in northeastern Japan subduction zone. *Tectonophysics*,
- 481 *572-573*, 38 - 46. doi: <https://doi.org/10.1016/j.tecto.2011.09.019>
- 482 Kanazawa, T., & Hasegawa, A. (1997). Ocean-bottom observatory for earthquakes
- 483 and tsunami off sanriku, north-east japan using submarine cable. *Interna-*
- 484 *tional Workshop on Scientific Use of Submarine Cables, Comm. for Sci.*
- 485 *Use of Submarine Cables, Okinawa, Japan, 1997*, 208-209. Retrieved from
- 486 <https://ci.nii.ac.jp/naid/10030183328/en/>
- 487 Kanbayashi, Y., & Ichikawa, M. (1977). A method for determining magnitude of
- 488 shallow earthquakes occurring in and near japan. *Quart. J. Seism.*, *41*, 57–61.
- 489 Kennett, B. (2015). Lithosphere–asthenosphere p-wave reflectivity across aus-
- 490 tralia. *Earth and Planetary Science Letters*, *431*, 225 - 235. Retrieved from
- 491 <http://www.sciencedirect.com/science/article/pii/S0012821X15006147>
- 492 doi: <https://doi.org/10.1016/j.epsl.2015.09.039>
- 493 Kramer, S. (1996). *Geotechnical Earthquake Engineering*. Prentice Hall PTR.
- 494 Kubo, H., Nakamura, T., Suzuki, W., Dhakal, Y. P., Kimura, T., Kunugi, T., ...
- 495 Aoi, S. (2019, 04). GroundMotion Characteristics and Nonlinear Soil Re-
- 496 sponse Observed by DONET1 Seafloor Observation Network during the 2016
- 497 Southeast OffMie, Japan, Earthquake. *Bull. Seismol. Soc. Am.*, *109*(3),
- 498 976-986. Retrieved from <https://doi.org/10.1785/0120170296> doi:
- 499 10.1785/0120170296
- 500 Lellouch, A., Yuan, S., Spica, Z., Biondi, B., & Ellsworth, W. L. (2019). Seis-
- 501 mic velocity estimation using passive downhole distributed acoustic sens-
- 502 ing records: Examples from the san andreas fault observatory at depth. *J.*
- 503 *Geophys. Res. Solid Earth*, *124*(7), 6931-6948. Retrieved from [https://](https://agupubs.onlinelibrary.wiley.com/doi/abs/10.1029/2019JB017533)
- 504 agupubs.onlinelibrary.wiley.com/doi/abs/10.1029/2019JB017533 doi:
- 505 <https://doi.org/10.1029/2019JB017533>
- 506 Lior, I., Sladen, A., Rivet, D., Ampuero, J.-P., Hello, Y., Becerril, C., ... Chris-
- 507 tostos, M. (2021). On the Detection Capabilities of Underwater Distributed
- 508 Acoustic Sensing. *Journal of Geophysical Research: Solid Earth*, *126*(3),
- 509 e2020JB020925. doi: 10.1029/2020JB020925
- 510 Lobkis, O. I., & Weaver, R. L. (2003, Jun). Coda-wave interferometry in finite
- 511 solids: Recovery of *p*-to-*s* conversion rates in an elastodynamic billiard. *Phys.*
- 512 *Rev. Lett.*, *90*, 254302. Retrieved from [https://link.aps.org/doi/10.1103/](https://link.aps.org/doi/10.1103/PhysRevLett.90.254302)
- 513 [PhysRevLett.90.254302](https://link.aps.org/doi/10.1103/PhysRevLett.90.254302) doi: 10.1103/PhysRevLett.90.254302
- 514 Lyakhovskiy, V., Hamiel, Y., Ampuero, J.-P., & Ben-Zion, Y. (2009, 08). Non-linear
- 515 damage rheology and wave resonance in rocks. *Geophys. J. Int.*, *178*(2), 910-
- 516 920. Retrieved from <https://doi.org/10.1111/j.1365-246X.2009.04205.x>
- 517 doi: 10.1111/j.1365-246X.2009.04205.x
- 518 Martin, E. R., Lindsey, N. J., Ajo-Franklin, J. B., & Biondi, B. L. (2021). Introduc-
- 519 tion to interferometry of fiber-optic strain measurements. In *Distributed acous-*
- 520 *tic sensing in geophysics* (p. 111-129). American Geophysical Union (AGU).
- 521 Retrieved from [https://agupubs.onlinelibrary.wiley.com/doi/abs/10](https://agupubs.onlinelibrary.wiley.com/doi/abs/10.1002/9781119521808.ch9)
- 522 [.1002/9781119521808.ch9](https://agupubs.onlinelibrary.wiley.com/doi/abs/10.1002/9781119521808.ch9) doi: <https://doi.org/10.1002/9781119521808.ch9>
- 523 Mellors, R., Kilb, D., & Ajo-Franklin, J. B. (2022). An examination of das as a
- 524 possible earthquake early warning tool. In S. R. Letters (Ed.), *2022 seismologi-*
- 525 *cal society of america annual meeting, technical sessions*. Seismological Society
- 526 of America. Retrieved from [https://meetings.seismosoc.org/wp-content/](https://meetings.seismosoc.org/wp-content/uploads/2022/04/SRL2B.pdf)
- 527 [uploads/2022/04/SRL2B.pdf](https://meetings.seismosoc.org/wp-content/uploads/2022/04/SRL2B.pdf)
- 528 Minato, S., Tsuji, T., Ohmi, S., & Matsuoka, T. (2012). Monitoring seis-
- 529 mic velocity change caused by the 2011 tohoku-oki earthquake using am-
- 530 bient noise records. *Geophys. Res. Lett.*, *39*, L09309. Retrieved from
- 531 <http://dx.doi.org/10.1029/2012GL051405> doi: 10.1029/2012GL051405
- 532 Nakahara, H. (2015). Auto correlation analysis of coda waves from local earth-

- 533 quakes for detecting temporal changes in shallow subsurface structures: the
 534 2011 tohoku-oki, japan earthquake. *Pure Appl. Geophys.*, 172, 213–224.
 535 Retrieved from <http://dx.doi.org/10.1007/s00024-014-0849-0> doi:
 536 10.1007/s00024-014-0849-0
- 537 Nakamura, T., & Hayashimoto, N. (2018, 11). Rotation motions of cabled ocean-
 538 bottom seismic stations during the 2011 Tohoku earthquake and their ef-
 539 fects on magnitude estimation for early warnings. *Geophys. J. Int.*, 216(2),
 540 1413-1427. Retrieved from <https://doi.org/10.1093/gji/ggy502> doi:
 541 10.1093/gji/ggy502
- 542 Nakata, N., & Snieder, R. (2011). Near-surface weakening in japan after the 2011
 543 tohoku-oki earthquake. *Geophys. Res. Lett.*, 38, L17302. Retrieved from
 544 <http://dx.doi.org/10.1029/2011GL048800> doi: 10.1029/2011GL048800
- 545 Ohmi, S., Hirahara, K., Wada, H., & Ito, K. (2008). Temporal variations of crustal
 546 structure in the source region of the 2007 noto hanto earthquake, central
 547 japan, with passive image interferometry. *Earth, Planets and Space*, 60(10),
 548 1069–1074. Retrieved from <https://doi.org/10.1186/BF03352871> doi:
 549 10.1186/BF03352871
- 550 Ohsaki, Y. (1966). Niigata earthquakes, 1964 building damage and soil con-
 551 dition. *Soils and Foundations*, 6(2), 14-37. Retrieved from [https://](https://www.sciencedirect.com/science/article/pii/S0038080620326160)
 552 www.sciencedirect.com/science/article/pii/S0038080620326160 doi:
 553 https://doi.org/10.3208/sandf1960.6.2_14
- 554 Ostrovsky, L., & Johnson, P. (2001). Dynamic nonlinear elasticity in geomaterials.
 555 *Rivista del nuovo cemento*, 24(7), 1–46.
- 556 Pasqualini, D., Heitmann, K., TenCate, J. A., Habib, S., Higdon, D., & John-
 557 son, P. A. (2007). Nonequilibrium and nonlinear dynamics in berea and
 558 fontainebleau sandstones: Low-strain regime. *J. Geophys. Res. Solid Earth*,
 559 112(B1). Retrieved from [https://agupubs.onlinelibrary.wiley.com/doi/](https://agupubs.onlinelibrary.wiley.com/doi/abs/10.1029/2006JB004264)
 560 [abs/10.1029/2006JB004264](https://agupubs.onlinelibrary.wiley.com/doi/abs/10.1029/2006JB004264) doi: <https://doi.org/10.1029/2006JB004264>
- 561 Pham, T.-S., & Tkalčić, H. (2017). On the feasibility and use of teleseismic p wave
 562 coda autocorrelation for mapping shallow seismic discontinuities. *J. Geophys.*
 563 *Res. Solid Earth*, 122, 3776-3791. doi: 10.1002/2017JB013975
- 564 Qin, L., Ben-Zion, Y., Bonilla, L. F., & Steidl, J. H. (2020). Imaging and monitoring
 565 temporal changes of shallow seismic velocities at the garner valley near anza,
 566 california, following the m7.2 2010 el mayor-cucapah earthquake. *J. Geophys.*
 567 *Res. Solid Earth*, 125(1), e2019JB018070. (e2019JB018070 2019JB018070) doi:
 568 <https://doi.org/10.1029/2019JB018070>
- 569 Quigley, M. C., Bastin, S., & Bradley, B. A. (2013). Recurrent liquefaction in
 570 christchurch, new zealand, during the canterbury earthquake sequence. *Geol-*
 571 *ogy*, 41, 419. Retrieved from [+http://dx.doi.org/10.1130/G33944.1](http://dx.doi.org/10.1130/G33944.1) doi:
 572 10.1130/G33944.1
- 573 Régnier, J., Cadet, H., Bonilla, L. F., Bertrand, E., & Semblat, J. (2013). As-
 574 sessing nonlinear behavior of soils in seismic site response: Statistical anal-
 575 ysis on kiknet strongmotion data assessing nonlinear behavior of soils in
 576 seismic site response. *Bull. Seismol. Soc. Am.*, 103, 1750. Retrieved from
 577 [+http://dx.doi.org/10.1785/0120120240](http://dx.doi.org/10.1785/0120120240) doi: 10.1785/0120120240
- 578 Remillieux, M. C., Ulrich, T. J., Goodman, H. E., & Ten Cate, J. A. (2017).
 579 Propagation of a finite-amplitude elastic pulse in a bar of berea sandstone:
 580 A detailed look at the mechanisms of classical nonlinearity, hysteresis, and
 581 nonequilibrium dynamics. *J. Geophys. Res. Solid Earth*, 122(11), 8892-8909.
 582 Retrieved from [https://agupubs.onlinelibrary.wiley.com/doi/abs/](https://agupubs.onlinelibrary.wiley.com/doi/abs/10.1002/2017JB014258)
 583 [10.1002/2017JB014258](https://agupubs.onlinelibrary.wiley.com/doi/abs/10.1002/2017JB014258) doi: <https://doi.org/10.1002/2017JB014258>
- 584 Sanchez-Sesma, F. J. (1987). Site effects on strong ground motion. *Soil*
 585 *Dynamics and Earthquake Engineering*, 6(2), 124-132. Retrieved from
 586 <https://www.sciencedirect.com/science/article/pii/0267726187900224>
 587 doi: [https://doi.org/10.1016/0267-7261\(87\)90022-4](https://doi.org/10.1016/0267-7261(87)90022-4)

- 588 Sawazaki, K., Sato, H., Nakahara, H., & Nishimura, T. (2006). Temporal change in
589 site response caused by earthquake strong motion as revealed from coda spec-
590 tral ratio measurement. *Geophys. Res. Lett.*, *33*(21). Retrieved from [https://](https://agupubs.onlinelibrary.wiley.com/doi/abs/10.1029/2006GL027938)
591 agupubs.onlinelibrary.wiley.com/doi/abs/10.1029/2006GL027938 doi:
592 <https://doi.org/10.1029/2006GL027938>
- 593 Saygin, E., Cummins, P. R., & Lumley, D. (2017). Retrieval of the P wave reflect-
594 ivity response from autocorrelation of seismic noise: Jakarta Basin, Indonesia.
595 *Geophys. Res. Lett.*, *44*, 792–799. doi: 10.1002/2016GL071363
- 596 Schimmel, M., & Paulssen, H. (1997, 08). Noise reduction and detection of weak,
597 coherent signals through phase-weighted stacks. *Geophys. J. Int.*, *130*, 497–505.
598 doi: 10.1111/j.1365-246X.1997.tb05664.x
- 599 Sens-Schönfelder, C., & Wegler, U. (2006). Passive image interferometry and
600 seasonal variations of seismic velocities at merapi volcano, indonesia. *Geo-*
601 *phys. Res. Lett.*, *33*, L21302. Retrieved from [http://dx.doi.org/10.1029/](http://dx.doi.org/10.1029/2006GL027797)
602 [2006GL027797](http://dx.doi.org/10.1029/2006GL027797) doi: 10.1029/2006GL027797
- 603 Shinohara, M., Yamada, T., Akuhara, T., Mochizuki, K., & Sakai, S. (2022).
604 Performance of seismic observation by distributed acoustic sensing tech-
605 nology using a seafloor cable off sanriku, japan. *Front. Mar. Sci.* doi:
606 <https://doi.org/10.3389/fmars.2022.844506>
- 607 Shinohara, M., Yamada, T., Uehira, K., Sakai, S., Shiobara, H., & Kanazawa, T.
608 (2021). Development and operation of an ocean bottom cable seismic and
609 tsunami (obcst) observation system in the source region of the tohoku-oki
610 earthquake. *Earth and Space Science*, *8*(3), e2020EA001359. Retrieved
611 from [https://agupubs.onlinelibrary.wiley.com/doi/abs/10.1029/](https://agupubs.onlinelibrary.wiley.com/doi/abs/10.1029/2020EA001359)
612 [2020EA001359](https://agupubs.onlinelibrary.wiley.com/doi/abs/10.1029/2020EA001359) (e2020EA001359 2020EA001359) doi: [https://doi.org/10.1029/](https://doi.org/10.1029/2020EA001359)
613 [2020EA001359](https://doi.org/10.1029/2020EA001359)
- 614 Spica, Z. J., Castellanos, J. C., Viens, L., Nishida, K., Akuhara, T., Shinohara, M.,
615 & Yamada, T. (2022). Subsurface imaging with ocean-bottom distributed
616 acoustic sensing and water phases reverberations. *Geophys. Res. Lett.*, *49*(2),
617 e2021GL095287. doi: <https://doi.org/10.1029/2021GL095287>
- 618 Spica, Z. J., Nishida, K., Akuhara, T., Pétrélis, F., Shinohara, M., & Yamada, T.
619 (2020). Marine sediment characterized by ocean-bottom fiber-optic seis-
620 mology. *Geophys. Res. Lett.*, *47*(16), e2020GL088360. (e2020GL088360
621 10.1029/2020GL088360) doi: <https://doi.org/10.1029/2020GL088360>
- 622 Spica, Z. J., Pertou, M., Martin, E. R., Beroza, G. C., & Biondi, B. (2020). Urban
623 seismic site characterization by fiber-optic seismology. *Journal of Geophysical*
624 *Research: Solid Earth*, *125*(3), e2019JB018656. doi: 10.1029/2019JB018656
- 625 Takagi, R., Okada, T., Nakahara, H., Umino, N., & Hasegawa, A. (2012). Co-
626 seismic velocity change in and around the focal region of the 2008 Iwate-
627 Miyagi Nairiku earthquake. *J. Geophys. Res. Solid Earth*, *117*, B06315. doi:
628 [10.1029/2012JB009252](https://doi.org/10.1029/2012JB009252)
- 629 TenCate, J. A., Pasqualini, D., Habib, S., Heitmann, K., Higdon, D., & Johnson,
630 P. A. (2004, Aug). Nonlinear and nonequilibrium dynamics in geomaterials.
631 *Phys. Rev. Lett.*, *93*, 065501. Retrieved from [https://link.aps.org/doi/](https://link.aps.org/doi/10.1103/PhysRevLett.93.065501)
632 [10.1103/PhysRevLett.93.065501](https://link.aps.org/doi/10.1103/PhysRevLett.93.065501) doi: 10.1103/PhysRevLett.93.065501
- 633 Tork Qashqai, M., Saygin, E., & Kennett, B. (2019). Crustal imaging with Bayesian
634 inversion of teleseismic P wave coda autocorrelation. *Journal of Geophysical*
635 *Research: Solid Earth*, *124*(6), 5888–5906.
- 636 Ventosa, S., Schimmel, M., & Stutzmann, E. (2019, 05). Towards the Processing
637 of Large Data Volumes with Phase CrossCorrelation. *Seism. Res. Lett.*, *90*(4),
638 1663–1669. Retrieved from <https://doi.org/10.1785/0220190022> doi: 10
639 .1785/0220190022
- 640 Viens, L., Denolle, M. A., Hirata, N., & Nakagawa, S. (2018). Complex near-surface
641 rheology inferred from the response of greater tokyo to strong ground mo-
642 tions. *J. Geophys. Res. Solid Earth*, *123*, 5710–5729. Retrieved from [https://](https://doi.org/10.1029/2017JB014000)

- 643 agupubs.onlinelibrary.wiley.com/doi/abs/10.1029/2018JB015697 doi:
644 10.1029/2018JB015697
- 645 Viens, L., Jiang, C., & Denolle, M. A. (2022, 04). Imaging the Kanto Basin seis-
646 mic basement with earthquake and noise autocorrelation functions. *Geophys.*
647 *J. Int.*, *230*(2), 1080-1091. Retrieved from <https://doi.org/10.1093/gji/ggac101>
648 doi: 10.1093/gji/ggac101
- 649 Viens, L., Perton, M., Spica, Z. J., Nishida, K., Shinohara, M., & Tomoaki, Y.
650 (2022). *Understanding surface-wave modal content for high-resolution imag-*
651 *ing of submarine sediments with distributed acoustic sensing.* Retrieved from
652 <https://doi.org/10.31223/X5MW7M> doi: 10.31223/X5MW7M
- 653 Wang, H. F., Zeng, X., Miller, D. E., Fratta, D., Feigl, K. L., Thurber, C. H., &
654 Mellors, R. J. (2018, 03). Ground motion response to an ML 4.3 earthquake
655 using co-located distributed acoustic sensing and seismometer arrays. *Geophys.*
656 *J. Int.*, *213*(3), 2020-2036. doi: 10.1093/gji/ggy102
- 657 Wapenaar, K. (2003). Synthesis of an inhomogeneous medium from its acoustic
658 transmission response. *Geophysics*, *68*, 1756–1759. doi: [https://doi.org/10](https://doi.org/10.1190/1.1620649)
659 [.1190/1.1620649](https://doi.org/10.1190/1.1620649)
- 660 Wegler, U., Nakahara, H., Sens-Schönfelder, C., Korn, M., & Shiomi, K. (2009).
661 Sudden drop of seismic velocity after the 2004 mw 6.6 mid-niigata earth-
662 quake, japan, observed with passive image interferometry. *J. Geophys. Res.*
663 *Solid Earth*, *114*, B06305. Retrieved from [http://dx.doi.org/10.1029/](http://dx.doi.org/10.1029/2008JB005869)
664 [2008JB005869](http://dx.doi.org/10.1029/2008JB005869) doi: 10.1029/2008JB005869
- 665 Wen, K.-L., Beresnev, I. A., & Yeh, Y. T. (1995). Investigation of non-linear
666 site amplification at two downhole strong ground motion arrays in taiwan.
667 *Earthquake Engineering & Structural Dynamics Structural Dynamics*, *24*, 313–
668 324. Retrieved from <http://dx.doi.org/10.1002/eqe.4290240302> doi:
669 [10.1002/eqe.4290240302](http://dx.doi.org/10.1002/eqe.4290240302)
- 670 Yang, Y., Atterholt, J. W., Shen, Z., Muir, J. B., Williams, E. F., & Zhan, Z.
671 (2022). Sub-kilometer correlation between near-surface structure and ground
672 motion measured with distributed acoustic sensing. *Geophys. Res. Lett.*, *49*,
673 e2021GL096503. Retrieved from [https://agupubs.onlinelibrary.wiley](https://agupubs.onlinelibrary.wiley.com/doi/abs/10.1029/2021GL096503)
674 [.com/doi/abs/10.1029/2021GL096503](https://agupubs.onlinelibrary.wiley.com/doi/abs/10.1029/2021GL096503) (e2021GL096503 2021GL096503) doi:
675 <https://doi.org/10.1029/2021GL096503>
- 676 Yates, A. S., Savage, M. K., Jolly, A. D., Caudron, C., & Hamling, I. J. (2019).
677 Volcanic, coseismic, and seasonal changes detected at white island (whakaari)
678 volcano, new zealand, using seismic ambient noise. *Geophys. Res. Lett.*, *46*(1),
679 99-108. Retrieved from [https://agupubs.onlinelibrary.wiley.com/doi/](https://agupubs.onlinelibrary.wiley.com/doi/abs/10.1029/2018GL080580)
680 [abs/10.1029/2018GL080580](https://agupubs.onlinelibrary.wiley.com/doi/abs/10.1029/2018GL080580) doi: <https://doi.org/10.1029/2018GL080580>
- 681 Zaitsev, V. Y., Nazarov, V. E., Tournat, V., Gusev, V. E., & Castagnede, B. (2005).
682 Luxemburg-gorky effect in a granular medium: Probing perturbations of the
683 material state via cross-modulation of elastic waves. *Europhysics Letters*, *70*,
684 607. Retrieved from <http://stacks.iop.org/0295-5075/70/i=5/a=607>
- 685 Zeng, X., Lancelle, C., Thurber, C., Fratta, D., Wang, H., Lord, N., ... Clarke, A.
686 (2017, 01). Properties of Noise CrossCorrelation Functions Obtained from a
687 Distributed Acoustic Sensing Array at Garner Valley, California. *Bull. Seis-*
688 *mol. Soc. Am.*, *107*(2), 603-610. Retrieved from [https://doi.org/10.1785/](https://doi.org/10.1785/0120160168)
689 [0120160168](https://doi.org/10.1785/0120160168) doi: 10.1785/0120160168